How to cite: *Angew. Chem. Int. Ed.* **2025**, *64*, e202510259
doi.org/10.1002/anie.202510259



Hydrogen Evolution Reaction **Very Important Paper**

Rationally Designed Asymmetric Pt—O—Cu Ligand to Stabilize Active Sites Towards Superior Industrial-Standard Alkaline Hydrogen Evolution

Minming Jiang, Jiang Xu, Qi Zhou, Yujie Chen,* Paul Munroe, Linlin Li, Zong-Han Xie, Yuping Wu, and Shengjie Peng**

Abstract: Developing efficient and durable Pt-based catalysts via interface engineering remains a critical yet challenging task for water electrolysis under high-pH conditions. Herein, we design a unique asymmetric Pt—O—Cu ligand at the $PtCu_2(111)/CuO(002)$ heterojunction interface to promote alkaline HER kinetics. This ligand balances the adsorption and desorption of H* on the Pt site by accelerating electron transfer at the interface while enhancing the adsorption of H_2O on the Cu site. Moreover, the strong d-d/sp hybridization and more delocalized d-DOS located at the Pt—O—Cu ligand enhance the interatomic interactions, which helps alleviate the dissolution and agglomeration of Pt and Cu atoms. As anticipated, the $PtCu_2/CuO$ requires ultra-low overpotentials of 10, 14 and 47 mV in, respectively, alkaline, acidic and neutral electrolytes to achieve a current density of 10 mA cm^{-2}. Even more surprising is that the $PtCu_2/CuO||RuO_2$ dual-electrode hydrolysis cell can stably operate at a high current density of 1 A cm^{-2} for more than 500 h in a simulated industrial environment, demonstrating significant potential for industrial applications. This work provides a new paradigm for the design of industrially relevant high-performance Pt-based alkaline hydrogen evolution catalytic materials.

Introduction

The electrocatalytic hydrogen evolution reaction (HER), driven by the growth in intermittent renewable energy (e.g., solar, wind and tidal energy), is an ideal strategy for large-scale production of green hydrogen (H_2) aiming to reduce, or even, replace traditional fossil fuels.[1–4] However, the distinct HER steps exhibited by Pt-based electrocatalysts in different pH media indicate that efficiency of their behaviour is strongly pH-dependent.[5,6] Unlike the direct formation of Pt—H_{ad} bonds via hydronium ions in acidic medium, the Pt-H_{ad} bonds in alkaline/neutral media originate from the dissociation of water, which is limited by the high energy barrier required to break strong H—OH bonds and thus causes the HER kinetics in high-pH media being two to three orders of magnitude slower than that in the acidic medium.[7–9] Additionally, the chemical/electrochemical dissolution that may occur in Pt-based electrocatalysts under industrial electrolysis environments (characterized by a high current density and corrosive environment) makes it still challenging to achieve long-term operation.[10] To solve the above problems, it is crucial to promote the efficiency of key steps, such as H_2O adsorption/dissociation, H^+ adsorption and H_2/OH^- desorption, through rationally electronic structure design of Pt-based electrocatalysts.

Currently, modification strategies including bimetallic alloying and heterojunction engineering have been widely used to improve the performance of Pt-based catalysts. The alloying of Pt with various transition metal (TM) elements can regulate the bonding strength between Pt-TM alloys and reaction intermediates through strong d-d orbital electron interactions, thereby enhancing the HER activity.[11] Among the numerous TM elements, copper (Cu) is an attractive alloying element due to its low price, abundant reserves, excellent conductivity, high chemical stability and good compatibility with Pt.[12–14] Yang et al. reported a robust functional structure integrated electrode (D-PtCu/CF) with abundant edge dislocations that can operate stably for 100 h at a voltage of 1.63 V and an industrial-grade current density of 500 mA cm^{-2}.[15] The in situ electrochemical experiments exhibit that edge dislocations can not only

[*] M. Jiang, Prof. J. Xu, Q. Zhou, Prof. L. Li
College of Materials Science and Technology, Nanjing University of Aeronautics and Astronautics, Nanjing 210016, China
E-mail: xujiang73@nuaa.edu.cn

Prof. Y. Chen, Prof. Z.-H. Xie
School of Mechanical Engineering, University of Adelaide, Adelaide, SA 5005, Australia
E-mail: yujie.chen@adelaide.edu.au

Prof. P. Munroe
School of Materials Science and Engineering, University of New South Wales, NSW 2052, Australia

Prof. Y. Wu, Prof. S. Peng
Confucius Energy Storage Lab, School of Energy and Environment & Z Energy Storage Center, Southeast University, Nanjing 211189, China
E-mail: pengshengjie@seu.edu.cn

Prof. S. Peng
Shaoxing Research Institute of Renewable Energy and Molecular Engineering, Shanghai Jiao Tong University, Shaoxing 312000, P.R. China

Additional supporting information can be found online in the Supporting Information section

© 2025 Wiley-VCH GmbH

enhance the intrinsic catalytic activity of Pt atoms, but also effectively increase the number of Cu active sites available for hydrogen adsorption, thereby synergistically accelerating the HER kinetics. The construction of heterojunction Pt-based electrocatalysts is also helpful for introducing varied catalytic active sites and adjusting the electronic structure.[16,17] For instance, Lu et al. obtained a Pt_2W/WO_3 heterostructure using electrochemical co-deposition, which showed a significantly better HER overpotential than commercial Pt/C electrocatalysts at the current density of 500 mA cm^{-2}.[18] Further density functional theory (DFT) calculations indicate that the synergistic effect of Pt_2W and WO_3 strongly promotes the rapid desorption of hydrogen. In addition, Hui et al. achieved excellent HER activity and durability of more than 400 h at a current density of 1000 mA cm^{-2} by synthesizing oxygen vacancy-rich Pt/NiO_x-O_V three-dimensional quasi-parallel heterostructures, and the corresponding DFT calculations reveal the regulation for the d-band center of electron-rich Pt by NiO_x-O_V.[19] The existence form of electrocatalysts has a great influence on their performance in practical application processes. Traditionally, electrocatalysts need to be dispersed onto conductive substrates using polymer binders, which affects the overall conductivity and reduces the electrocatalytic activity. On the contrary, the self-supporting electrodes formed by in situ integration of electrocatalysts on carbon materials or metal carriers effectively avoid the use of binders, eliminating the hidden dangers of binder deactivation and low conductivity under high current densities.[20,21] Therefore, developing efficient and stable self-supporting electrodes is very important to reduce the cost of water splitting.

Previous studies have demonstrated that the HER performance of Pt metal catalysts is closely related to its crystal orientation, as different facets expose distinct active sites. Among them, the Pt(111) crystal plane exhibits superior activity due to its optimal hydrogen adsorption energy and stable surface structure.[22–24] In this study, we screened out a PtCu alloy with a Pt:Cu atomic ratio of 1:2 (denoted as $PtCu_2$) exhibiting the best HER performance via DFT method, and subsequently designed the $PtCu_2(111)/CuO(104)$ heterojunction structure to further improve its performance. Experimentally, the $PtCu_2$/CuO coating was deposited on a commercially pure Ti substrate using the dual-cathode sputtering deposition method to prepare a self-supporting electrode. Multiple characterization methods confirmed that the as-prepared coating has numerous heterojunction interfaces composed of $PtCu_2(111)$ and CuO(002) crystal planes, which is consistent with the theoretical design. Benefiting from the unique asymmetric hexagonal ring structure at the $PtCu_2$/CuO heterojunction interface, which regulates the electronic structure of the catalytic site and the equilibrium adsorption/desorption of intermediate reactants, the as-prepared $PtCu_2$/CuO heterojunction coating shows excellent catalytic activity in the pH-universal HER process. More importantly, the strong interatomic interaction brought about by the asymmetric Pt—O—Cu ligand greatly alleviates the dissolution and aggregation of Pt and Cu atoms, thus showing strong long-term stability at a large current density [After running for 500 h at a current density of 1 A cm^{-2}, current density only decreased by 5.6% in a simulated industrial environment (30% KOH, 80 °C)].

Results and Discussion

DFT calculation is regarded as an effective means for designing catalysts and predicting their performance. On the Pt(111) surface, PtCu(111), $PtCu_2(111)$ and $PtCu_3(111)$ models were constructed by gradually increasing the proportion of Cu atoms. Considering that the active atom is easily affected by the surrounding coordination,[25,26] the HER performance of the hexagonal ring structure with different Pt/Cu ratios centered on the Pt atom in the above four models is calculated, as shown in Figure 1a. The adsorption energy for H_2O (ΔE_{H2O}) on the surface of an electrocatalytic material is a crucial factor affecting the alkaline/neutral HER activity (during the Volmer step).[27] Figure 1b compares the ΔE_{H2O} values at different adsorption sites in the various models. Obviously, H_2O molecules are more strongly adsorbed on the Cu sites than on the Pt sites, indicating that the introduction of Cu atoms improves H_2O adsorption efficiency. The corresponding adsorption configurations show that the enhanced adsorption of H_2O by Cu sites leads to shortened bonding distances between them (Figure S1). Notably, the E_{H2O} value at the Cu site on $PtCu_2(111)$ is larger than that on PtCu(111) and $PtCu_3(111)$. Generally, a stronger H_2O adsorption is beneficial for subsequent water dissociation.[28] To verify this, the reaction energy barriers of the water-dissociating transition state (TS) at the optimal H_2O adsorption sites on the four model surfaces are calculated and shown in Figure 1d. As expected, the $PtCu_2(111)$ surface exhibits a water dissociation energy barrier (0.41 eV) smaller than that of Pt(111) (0.88 eV), PtCu(111) (0.69 eV) and $PtCu_3(111)$ (0.62 eV). To evaluate the Heyrovsky/Tafel step rates of four models over a wide-pH environment, the Gibbs free energy difference (ΔG_{H^*}) values of hydrogen proton (H*) adsorption/desorption on the Pt-central sites were calculated. As shown in Figure 1e, $PtCu_2(111)$ has a ΔG_{H^*} value closer to 0 eV than Pt(111), PtCu(111) and $PtCu_3(111)$, which is beneficial for more balanced H* adsorption and desorption.[29] Therefore, the HER activity of $PtCu_2(111)$ is better than that of Pt(111), PtCu(111) and $PtCu_3(111)$.

According to the above DFT calculation results, the best-performing $PtCu_2(111)$ was coupled with CuO(002) through heterojunction engineering to construct a $PtCu_2(111)/CuO(002)$ model with a lattice matching error of less than 5% (Figure 1a). In this model, the Pt atom remains the central coordination site, surrounded by Pt, Cu and O atoms forming an asymmetric hexagonal ring-like structure that extends across multiple atomic layers. Within this configuration, the O atom acts as a bridging species to connect Pt and Cu atoms, chemically linking Pt and Cu through coordinated bonding (Figure S2). Compared with $PtCu_2(111)$, the Cu sites belonging to the CuO side in $PtCu_2(111)/CuO(002)$ show a stronger H_2O adsorption effect (Figure 1b). The analysis of PDOS results indicates that the gap value between the Cu site in the CuO side

© 2025 Wiley-VCH GmbH

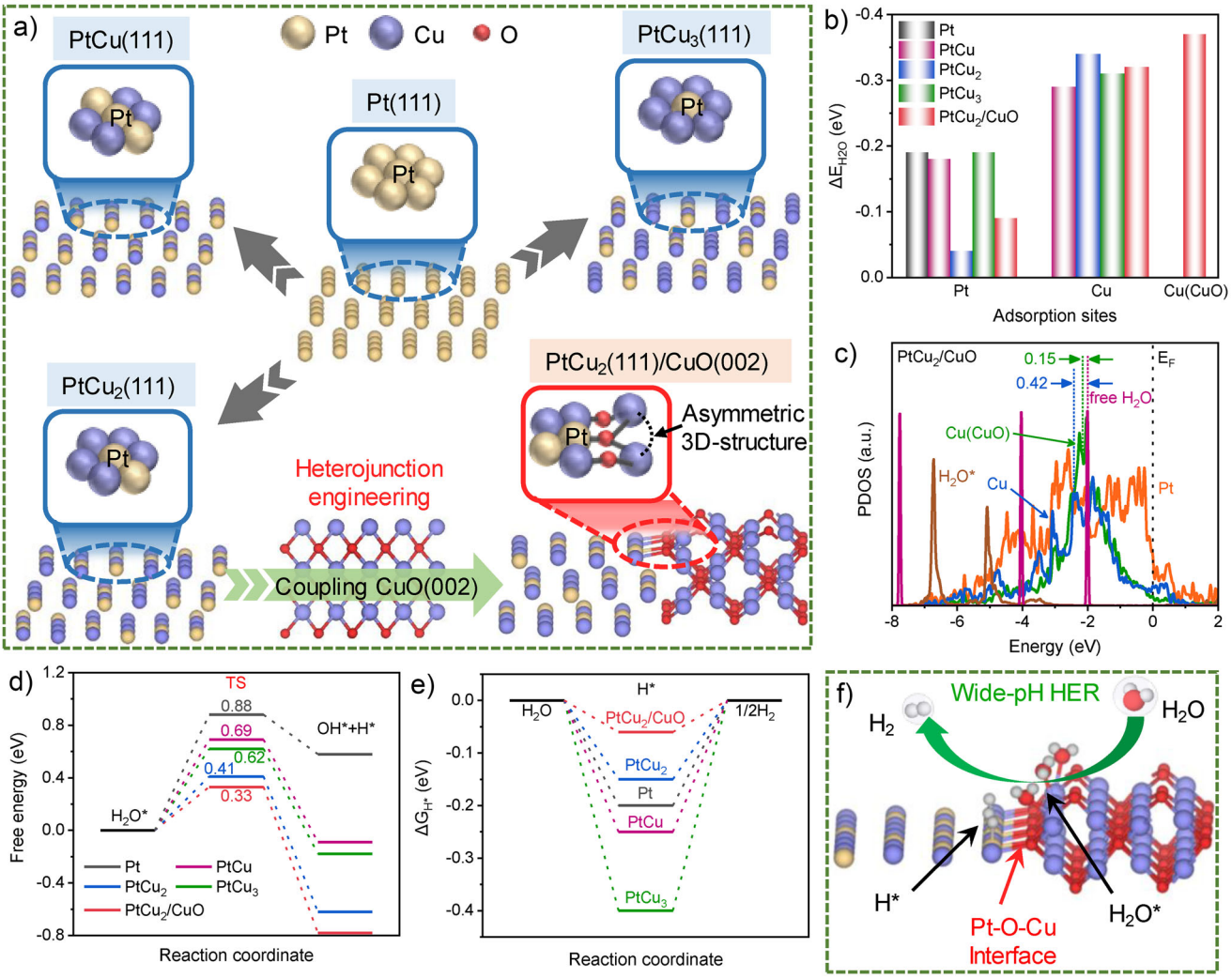

Figure 1. a) Designed atomic models for Pt(111), PtCu(111), $PtCu_2$(111), $PtCu_3$(111) and $PtCu_2$(111)/CuO(002). b) Adsorption energies for H_2O molecules on adsorption sites of different model surfaces. c) The PDOS for H_2O adsorption on $PtCu_2$/CuO. d) Activation barriers for water splitting and e) Gibbs free energies for hydrogen adsorption on the Pt, PtCu, $PtCu_2$, $PtCu_3$ and $PtCu_2$/CuO surfaces. f) The Cu-Pt—O—Cu interface in $PtCu_2$/CuO accelerates water splitting rate to achieve excellent HER performance in a wide-pH range.

(0.15 eV) and free H_2O is smaller than that of the Cu site on the $PtCu_2$ side (0.42 eV), which promotes the adsorbed H_2O* to transition to a deeper level (Figure 1c). Moreover, the $PtCu_2$(111)/CuO(002) surface exhibits the lowest water dissociation energy barrier (0.33 eV), implying that the designed heterojunction accelerates the formation rate of H* and thus accelerates HER kinetics (Figure 1d). For the ΔG_{H^*} value, the $PtCu_2$(111)/CuO(002) shows a significantly increased value (Figure 1e), resulting in the weakened adsorption and accelerated desorption of H* by the Pt-central site and ultimately achieves the rapid release of H_2, which can be attributed to the downward d-band center causing more electrons filling in the anti-bonding state (Figure S3).[30] Combined with the above calculation results, the Cu site located on the CuO side in the $PtCu_2$(111)/CuO(002) heterostructure exhibits significantly enhanced H_2O adsorption as well as rapid water dissociation behavior, providing sufficient H* sources for the rapid recombination of H_2 at the Pt site. This clear division in roles at the heterojunction interface ensures the stable occurrence of high HER activity in a wide-pH medium.

To verify the theoretical calculation results, a self-supporting $PtCu_2$/CuO heterojunction coating was deposited in a dual-cathode sputtering deposition system. As shown in Figure 2a, a precise proportion of Pt, Cu and CuO powders was first ball milled to provide a uniform composition, and then the mixture was pressed into a target. Finally, $PtCu_2$/CuO coatings were deposited on commercially pure-Ti substrates using the sputtering deposition technique. Details of the target preparation process and coating deposition parameters are provided in the Methods section. For comparison, the individual PtCu alloy coating with a Pt:Cu atomic ratio of 1:2 (hereinafter referred to as $PtCu_2$) and individual CuO coating were also prepared via the same process. Scanning electron microscope (SEM) analysis revealed that the surface of the $PtCu_2$/CuO coating exhibits a morphology characterized by a mixture of grooves and small protrusions. In contrast,

© 2025 Wiley-VCH GmbH

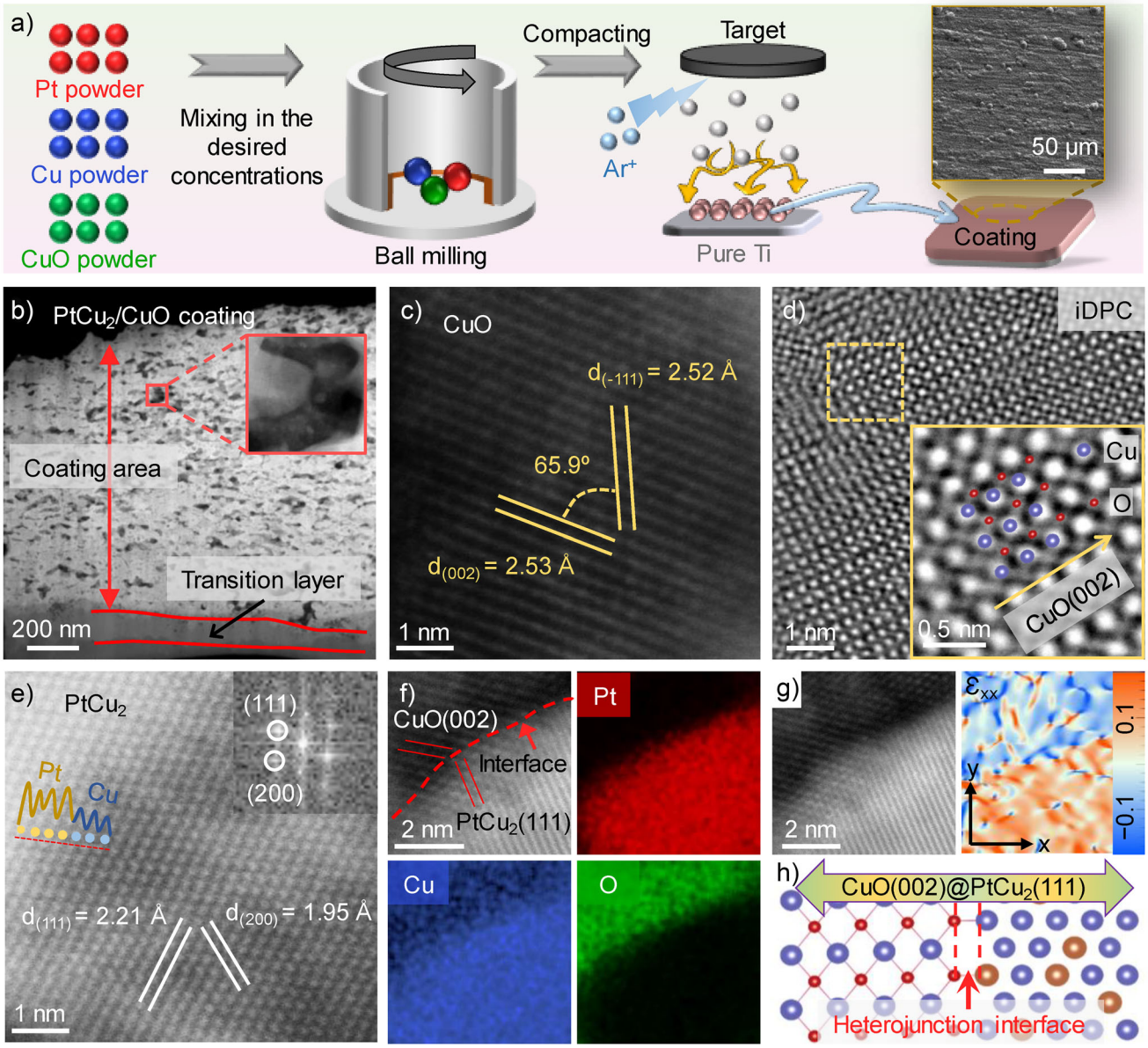

Figure 2. a) Sputtering deposition process diagram of the $PtCu_2$/CuO coating, and the corresponding SEM morphology. b) Cross-sectional HAADF-STEM image of the $PtCu_2$/CuO coating including the Ti substrate. c) HAADF-STEM and d) iDPC images located in the CuO region of the $PtCu_2$/CuO heterojunction. e) The HAADF-STEM image located in the $PtCu_2$ region of the $PtCu_2$/CuO heterojunction. f) HAADF-STEM image and corresponding STEM-EDS element maps of the $PtCu_2$/CuO heterojunction interface, as well as g) the GPA strain distribution along the ε_{xx}. h) Heterojunction interface model composed of CuO(002) and $PtCu_2$(111).

the surfaces of the CuO and $PtCt_2$ coatings are dominated by small protrusions and grooves, respectively (Figure S4). Furthermore, the formation of the $PtCu_2$/CuO heterojunction can significantly reduce the contact angle and enhance the hydrophilicity of the coating surface, thereby reducing the hydrolysis activation energy (Figure S5), which can be attributed to the increase in surface energy.[31,32]

A cross-sectional transmission electron microscope (TEM) sample was prepared using focused ion beam (FIB) microscopy (Figure S6). The high-angle annular dark-field transmission electron microscope (HAADF-STEM) image reveals a clear contrast between bright and dark phases within the coating (Figure 2b). Additionally, a clear transition layer can be seen between the coating and the Ti substrate. Combined with EDS-mapping analysis (Figure S7), the bright phase in the coating is enriched in Pt and Cu, the dark phase is enriched in Cu and O, while the transition layer contains Pt, Cu and Ti. For the bright and dark phase regions in the coating, the high-resolution EDS maps are consistent with these observations (Figure S8). Notably, the presence of a transition layer ensures a strong bond between the coating and the substrate, effectively avoiding detachment of the coating during the long-term HER environment. Additionally, the analysis of EDS line-scan data reveals

© 2025 Wiley-VCH GmbH

that the atomic ratio of Pt and Cu is close to 1:2, while the atomic ratio of Cu and O is close to 1:1 (Figure S9). Therefore, it can be suggested that the prepared coating is composed of a metal phase ($PtCu_2$) and a metal oxide phase (CuO).

To further analyze the composition of different phases in the coating, high-resolution TEM imaging of the oxide phase, metal phase and heterojunction interface was performed. As shown in the HAADF-STEM image of the oxide phase presented in Figure 2c, the measured spacings of the two crystal planes visible are 2.52 and 2.53 Å, which correspond, respectively, to the (−111) and (002) crystal planes of the CuO monoclinic crystal structure.[33] The atomic arrangement observed in the integrated differential phase contrast (iDPC) image (Figure 2d) further confirms the arrangement of the Cu and O atoms is clearly visible, consistent with the CuO(002) model. For the $PtCu_2$ metal phase, as shown in Figure 2e, the spacings between the adjacent lattice fringes are measured to be 2.21 and 1.95 A, corresponding to the (111) and (200) crystal planes of face-centered-cubic (FCC) metal phase, respectively. The integrated pixel intensity results derived along the red dotted line show a significant intensity difference due to the large mass difference between the Pt and Cu. Subsequently, a $PtCu_2$(111)||CuO(002) interphase orientation relationship was determined from the HAADF-STEM image of the interface, as shown in Figure 2f. The corresponding STEM-EDS maps and EDS line-scan results confirm the expected distribution of elements in each phase (Figures 2f and S10). Furthermore, the strain distribution image at the heterojunction interface based on the geometric phase analysis (GPA) method presents obvious strain fluctuations (Figure 2g), in which the FCC-phase with a smaller lattice parameter suffers the tensile stress, while the CuO phase with a bigger lattice parameter is subjected the compressive stress, which is essential to enhance the interatomic covalency and thus improve the catalytic activity.[34] X-ray diffraction (XRD) patterns also confirm the coexistence of the CuO and FCC metal phases in the $PtCu_2$/CuO coating (Figure S11). It is worth noting that the diffraction peak for $PtCu_2$ are between the theoretical peak positions of elemental Pt (JCPDS 87-0647) and elemental Cu (JCPDS 70-3038), which is caused by the lattice contraction between Pt and Cu atoms with different sizes.[35,36] Using the semi-quantitative reference intensity ratio (RIR) method, the phase constitution of the coating is estimated to be 66.2 wt.% CuO phase and 33.8 wt.% of a $PtCu_2$ metallic phase, respectively, closely matching the designed ratio in the $PtCu_2$/CuO target. Based on these experimental results, a heterojunction coating containing a CuO(002)/$PtCu_2$(111) interface was successfully deposited on the commercially pure Ti substrate (Figure 2h).

X-ray photoelectron spectroscopy (XPS) was used to investigate the electronic interactions in the $PtCu_2$/CuO heterojunction. In the XPS fine spectrum for C 1s, the main peak (C—C) located at 284.8 eV serves as the calibration for the binding energies of other elements (Figure S12). For the $PtCu_2$ coating, in addition to exhibiting the main metallic Cu^0 and Pt^0, signals for Cu and Pt also show a small amount of high valence Cu^{2+} and Pt^{2+} states presumably due to oxidation (Figure S13). As shown in Figure 3a, the proportion of characteristic peaks belonging to Cu^{2+} on the $PtCu_2$/CuO coating increases markedly, and the three adjacent satellite peaks confirm the presence of CuO.[37] In addition, an increase in high valence Pt^{2+} states can also be observed in the $PtCu_2$/CuO coating (Figure 3b), which may be related to the interaction between Pt atoms in $PtCu_2$ and O atoms in CuO at the interface. From the XPS peak area ratio, the proportions of Pt^{2+} and Cu^{2+} increase, respectively, from 12.4% to 32.3% and from 16.0% to 57.1% after heterostructure formation (Table S1). This interaction also causes a positive shift in the binding energy of the Pt° characteristic peak, indicating that electrons can flow from the $PtCu_2$ phase to the CuO phase through the heterojunction interface. In the O 1s fine spectrum, two peaks belonging to O-M and adsorbed H_2O can be fitted (Figure S14).[38]

Evaluating the atomic coordination and valence state changes after the formation of the $PtCu_2$/CuO heterojunction using X-ray absorption spectroscopy (XAS) can help further understand the electronic interactions and bonding units at this interface.[39] Figure 3c displays the X-ray absorption near-edge structure (XANES) spectra for a series of Pt samples, where the intensity of the white line (WL) on the Pt L_3-edge corresponds to the transition from the occupied Pt $2p_{3/2}$ electrons to the empty $5d_{5/2}$ orbital. A higher intensity WL peak represents more 5d empty orbitals and a higher probability of electron transitions, thereby exhibiting a higher Pt oxidation state.[40] Obviously, the WL intensity for $PtCu_2$ is close to that for Pt foil, meaning that the Pt valence state of $PtCu_2$ is mainly metallic.[41] With the introduction of CuO, the WL intensity for $PtCu_2$/CuO is higher than that for Pt foil, but much lower than that for PtO_2, indicating that electrons will transfer from $PtCu_2$ to CuO through the heterojunction interface, and thus leading to an increase in Pt valence state, which is consistent with the XPS results. This conclusion is also supported by the nearly coincident absorption edge for $PtCu_2$ and Pt foil, as well as the high-energy shift for $PtCu_2$/CuO (inset in Figure 3c). For XANES spectra of the Cu K-edge, as illustrated in Figure 3d, Cu atoms located in $PtCu_2$ and $PtCu_2$/CuO exhibit metallic and oxidized states, respectively. In the corresponding extended X-ray absorption fine structure (EXAFS) spectra for the Pt L_3-edge and Cu K-edge, $PtCu_2$/CuO not only exhibits Pt—Pt/Cu and Cu—Pt/Cu bonds belonging to the metallic state, but also Pt—O and Cu—O bonds belonging to the oxidized state (Figure 3e,f). Moreover, additional Pt—O—Cu and Cu—O—Cu bonds are observed in the $PtCu_2$/CuO, which is consistent with the bonding behavior at the heterojunction interface model as predicted by DFT (Figure 3g). In addition to this experimental approach, the DFT method was also employed to evaluate the electron transfer at the interface of $PtCu_2$(111)/CuO(002) heterojunction interface. As shown in the planar average potential diagram for $PtCu_2$/CuO shown in Figure 3h, electrons on the $PtCu_2$ side with higher potential will readily flow towards CuO on the lower potential side. Meanwhile, the results of charge differential density (CDD) calculations and the corresponding Z-direction plane average CDD also indicate the depletion of electrons on the $PtCu_2$ side and accumulation of electrons on the CuO side due to this electron flow (Figure 3i). The corresponding

© 2025 Wiley-VCH GmbH

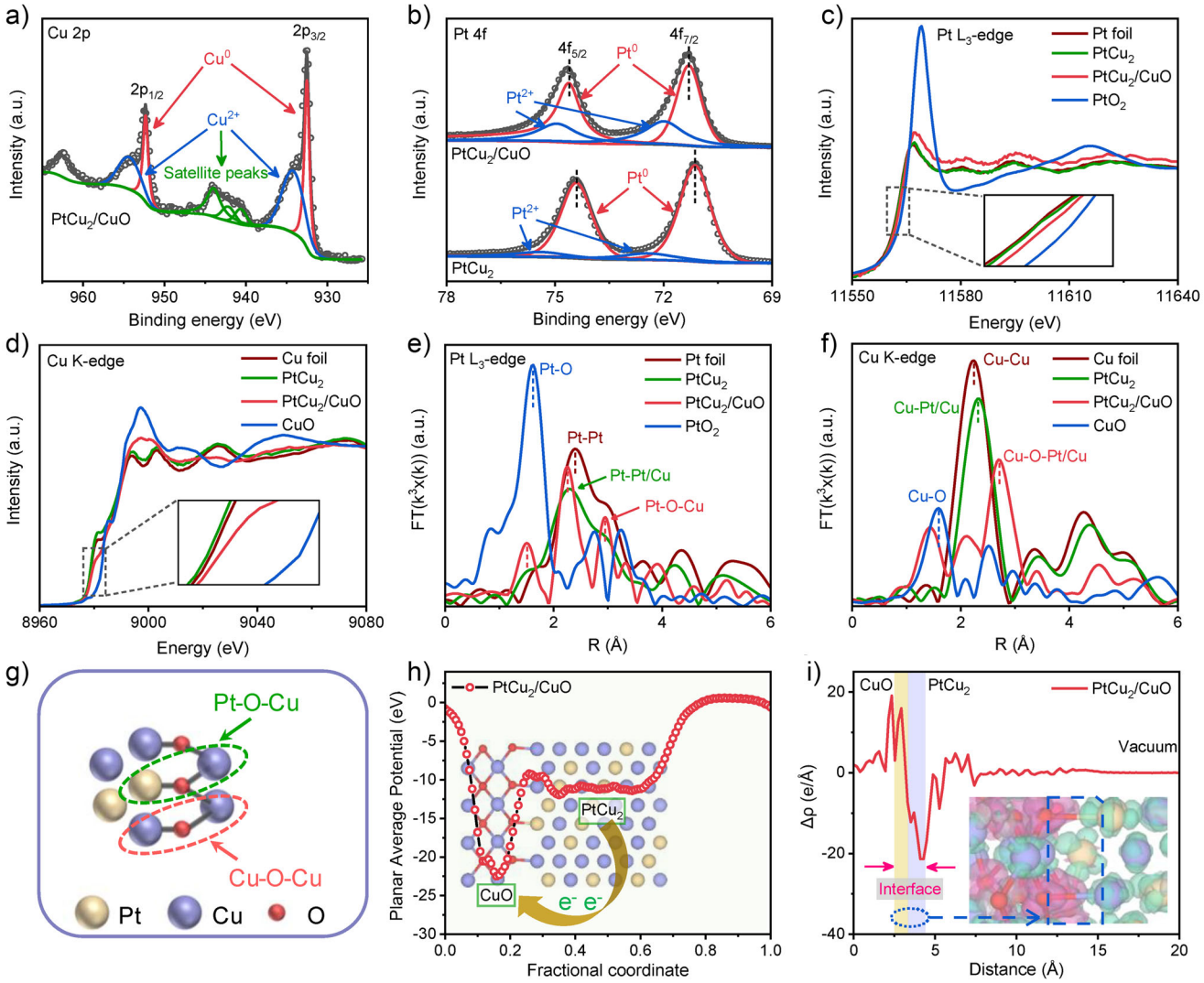

Figure 3. XPS fine spectra for the Cu 2p signal from the a) $PtCu_2/CuO$ coating, as well as the b) Pt 4f signal from the $PtCu_2/CuO$ and $PtCu_2$ coatings. c, d) normalized XANES and e, f) RSFs for the Pt L_3-edge and Cu K-edge obtained by Fourier transform k^2-weighted EXAFS results. g) Pt—O—Cu and Cu—O—Cu bonding relationship at the interface of $PtCu_2/CuO$ heterojunction. h) Planar average potential and i) Z-direction plane average CDD for the $PtCu_2/CuO$ heterojunction model. The green and red areas in the inset represent depletion and accumulation of charge, respectively.

electron depletion and accumulation amounts are 0.87 e and 0.90 e, respectively. This charge redistribution is conducive to improving chemical stability, optimizing the adsorption behavior of reaction intermediates, and improving interfacial conductivity, thereby enhancing the long-term stability of the electrocatalytic coating.[42] Therefore, by combining results from TEM, XPS, XAS and DFT, it is demonstrated that a unique asymmetric hexagonal ring structure containing metal ion bonds and covalent bonds in the prepared $PtCu_2/CuO$ heterojunction coating was successfully designed.

To confirm the advantages of the designed $PtCu_2/CuO$ in pH-universal HER, electrochemical tests were conducted in acidic (1 M KOH), neutral (1 M PBS) and alkaline (0.5 M H_2SO_4) solutions via the standard three-electrode configuration, and compared with $PtCu_2$, CuO and commercial 20 wt%-Pt/C. Considering the DFT prediction that the $PtCu_2/CuO$ heterojunction can effectively enhance the adsorption and dissociation of H_2O, the HER performance of the above-mentioned electrocatalytic materials in an alkaline environment was first evaluated. In the polarization curves obtained by linear sweep voltammetry (LSV), the $PtCu_2/CuO$ exhibits the best HER activity compared with other materials (Figure 4a). At current densities of 10 and 100 mA cm^{-2}, the overpotentials of $PtCu_2/CuO$ are only 10 and 46 mV, much lower than those of $PtCu_2$ (47 and 137 mV) and Pt/C (42 and 158 mV), as shown in Figure 4b. As an important parameter for studying the kinetics of electrocatalytic reactions, the Tafel slopes of different materials derived from LSV curves are compared in Figure 4c. The results indicate that $PtCu_2/CuO$ has the smallest Tafel slope (47.2 mV dec^{-1}), which suggests that the construction of heterojunctions can effectively accelerate the charge transfer kinetics during the HER processes. This is also demonstrated by the minimum charge

© 2025 Wiley-VCH GmbH

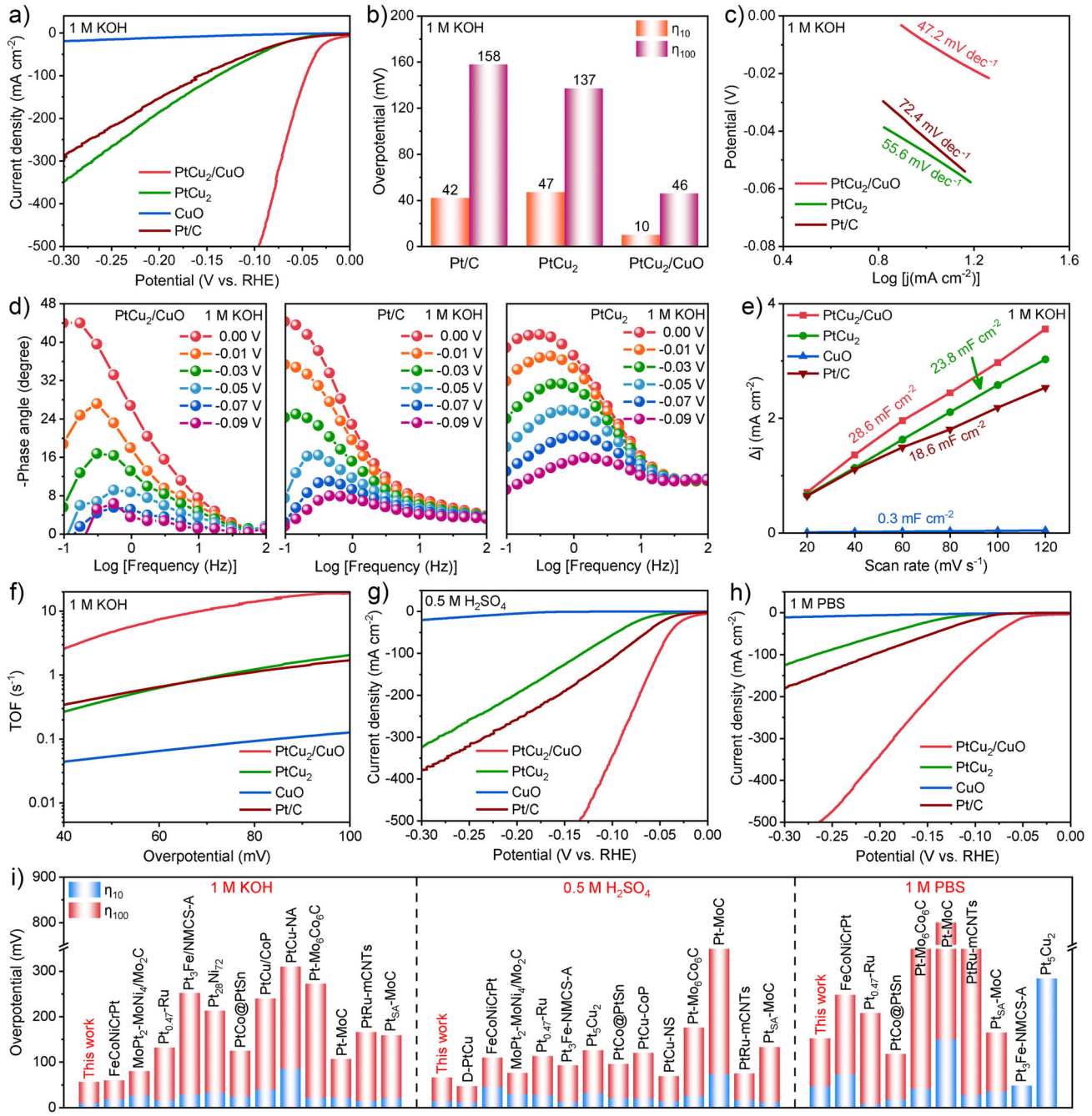

Figure 4. a) HER LSV curves and corresponding b) overpotentials and c) Tafel plots for different electrodes in 1 M KOH. d) EIS-Bode plots of $PtCu_2/CuO$, Pt/C and $PtCu_2$ in 1 M KOH at different HER overpotentials. e) C_{dl} values and f) TOF values for different electrodes. The HER LSV curves for different electrodes in g) 0.5 M H_2SO_4 and h) 1 M PBS. i) Overpotential comparison of the prepared $PtCu_2/CuO$ with the recently reported Pt-based HER catalysts in different solutions at 10 and 100 mA cm^{-2} current densities.

transfer resistance exhibited by $PtCu_2/CuO$ in the Nyquist plot from electrochemical impedance spectroscopy (EIS) (Figure S15). Furthermore, the response of $PtCu_2/CuO$, Pt/C and $PtCu_2$ to the low-frequency region of the EIS Bode plots at different HER potentials was compared to investigate the interface charge transfer between catalytic materials and electrolytes. As the potential increases, as shown in Figure 4d, the phase angle peak of $PtCu_2/CuO$ rapidly decreases, indicating a rapid charge transfer rate that favors the adsorption and desorption of reaction intermediates, ultimately accelerating the HER process.

The double-layer capacitance (C_{dl}) value obtained from the cyclic voltammetry (CV) curves with different scan rates was used to evaluate the electrochemical active surface area (ECSA) of the catalytic material (Figure S16). As shown in Figure 4e, $PtCu_2/CuO$ has the largest C_{dl} value compared to other materials, indicating the presence of the largest number of active sites on its surface. After normalizing

© 2025 Wiley-VCH GmbH

the LSV curves based on ECSA analysis, it is found that $PtCu_2$/CuO still exhibits significantly superior unit HER activity (Figure S17). Subsequently, the turnover frequencies (TOF), which represent the number of H_2 molecules produced per second at each active site during the HER process,[43] were used to evaluate the intrinsic activities of catalytic materials (Figure 4f). Clearly, $PtCu_2$/CuO exhibits the highest TOF values across the entire overpotential range of 40–100 mV, indicating its optimal intrinsic HER activity and can be attributed to the electronic structure regulation of the active site by the heterojunction.

In addition to the alkaline solution, the HER activities of $PtCu_2$/CuO and the reference materials in both acidic and neutral solutions were also explored. It is evident from the LSV curves presented in Figure 4g,h that $PtCu_2$/CuO evidently exhibits the best HER performance among all four catalytic materials, specifically, $PtCu_2$/CuO has the lowest overpotential at both 10 and 100 mV overpotentials (Figure S18). Similarly, the smaller Tafel slopes for $PtCu_2$/CuO in the corresponding Tafel plots indicate its rapid charge transfer kinetics (Figure S19). This is also demonstrated by the smaller capacitive loops for $PtCu_2$/CuO in both acidic and neutral solutions (Figure S20). It is worth noting that the Tafel slopes for $PtCu_2$/CuO in acidic (29.9 mV dec^{-1}) and alkaline (47.2 mV dec^{-1}) solutions differ significantly, corresponding to the Volmer-Tafel and Volmer-Heyrovsky rate determining steps, respectively.[44] In addition, the intrinsic catalytic activity between catalytic materials was compared by calculating ECSA and TOF values. Compared to $PtCu_2$ and Pt/C, $PtCu_2$/CuO exhibits the highest ECSA value and the best unit HER activity in both acidic (Figure S21) and neutral (Figure S22) solutions, indicating that it has the most catalytic active sites. Meanwhile, the leading TOF values for $PtCu_2$/CuO in the HER potential range relative to other materials demonstrate its excellent intrinsic catalytic activity (Figure S23). In addition, the mass activity of the $PtCu_2$/CuO coating at a 100 mV overpotential is, respectively, about 11, 3 and 5.5 times higher than that of Pt/C in 1 M KOH, 0.5 M H_2SO_4 and 1 M PBS electrolytes, showing better economic benefits (Figure S24). For direct comparison, the overpotential of $PtCu_2$/CuO, as well as recently reported values for other Pt-based electrocatalysts, in a pH-universal environment is shown in Figure 4i. The HER activity for $PtCu_2$/CuO is superior to most reported electrocatalysts, whether at a current density of 10 or 100 mA cm^{-2} (Table S2). Thus, the $PtCu_2$/CuO heterojunction in this work is able to improve the number of active sites and intrinsic activity, while accelerating charge transfer process, thereby achieving excellent pH-universal HER activity.

As is well known, for practical applications, long-term stability is another design focus of Pt-based electrocatalysts in addition to the high alkaline HER activity. In the time-dependent current density curves (i-t) for 10 h, the $PtCu_2$/CuO exhibits almost no attenuation of current density in all three electrolytes (Figure S25). In contrast, varying degrees of current density loss are observed for $PtCu_2$ and commercial Pt/C, indicating that the heterojunction coating prepared in this work has superior pH-universal catalytic stability. Subsequently, further comparisons were made between $PtCu_2$/CuO and commercial Pt/C using other durability tests. After 10 000-cycled CVs, the LSV curves for $PtCu_2$/CuO in the three electrolytes almost overlapped with the initial curves, indicating its excellent stability in redox reactions (Figure S26). In contrast, the commercial Pt/C exhibits significant performance degradation under the same conditions. Strikingly, as displayed in Figure 5a, $PtCu_2$/CuO only increases a small amount of overpotential after 100 h for a high current density (500 mA cm^{-2}) tested in a 1 M KOH electrolyte, and the high overlap LSV curves before and after testing (inset in Figure 5a) also indicate an effective slowing down of HER activity decay. However, the commercial Pt/C exhibits significant HER activity decay within less than 15 h of testing, and the corresponding LSV curves before and after testing also show evidence of this decay. The large stability difference between $PtCu_2$/CuO and commercial Pt/C mentioned above can also be observed in both 0.5 M H_2SO_4 and 1 M PBS electrolytes (Figure S27). Therefore, compared with commercial Pt/C electrodes prepared by a conventional slurry coating method, the heterojunction coating electrode prepared in this work has excellent industrial application prospects. This is further supported by XRD results (Figure S28), which confirm the structural integrity and phase stability of the $PtCu_2$/CuO coating after long-term HER testing across different pH environments, indicating strong resistance to phase degradation under operational conditions.

To reveal the origin of the excellent pH-universal durability of $PtCu_2$/CuO, a series of experimental characterizations and DFT calculations were conducted, with $PtCu_2$ as a reference. As shown by SEM analysis presented in Figure 5b, the morphology of the $PtCu_2$/CuO surface does not change significantly after alkaline long-term stability testing, while some damage was observed on the $PtCu_2$ surface, revealing the superiority of the heterostructure. The corresponding EDS-maps acquired from the damaged area show the presence of titanium arising from the substrate. That is, the substrate has become exposed due to delamination of the $PtCu_2$ coating. Similarly, $PtCu_2$/CuO also exhibits intact surface morphologies after long-term stability tests in both acidic and neutral conditions (Figure S29). Furthermore, damage was apparent on the surface of the $PtCu_2$ sample, as observed through SEM-EDS analysis (Figure S30). In addition, XPS spectra, acquired from $PtCu_2$/CuO after durability tests in different electrolytes, show that Pt still exists in a predominantly metallic state, with only a small amount of high-valence chemical states caused by the heterojunction (Figures 5c and S31). However, a large number of Pt^{4+} oxidation states are observed in the Pt 4f spectrum for $PtCu_2$, and this attenuation of low-valent Pt due to oxidation. This is a common reason for the inactivation of Pt-based materials in HER, which also indirectly indicates that the synergistic effect between $PtCu_2$ and CuO effectively prevents Pt oxidation.[45] The Pt L_3-edge in the XANES spectra show that there is no significant change in the spectra for $PtCu_2$/CuO before and after testing. However, $PtCu_2$ exhibits a right shift of the L_3-edge and an enhancement of the WL peak after testing, as shown in Figure 5d. In the corresponding EXAFS spectra, a peak belonging to the Pt-O bond can be clearly seen in $PtCu_2$ after testing, again

© 2025 Wiley-VCH GmbH

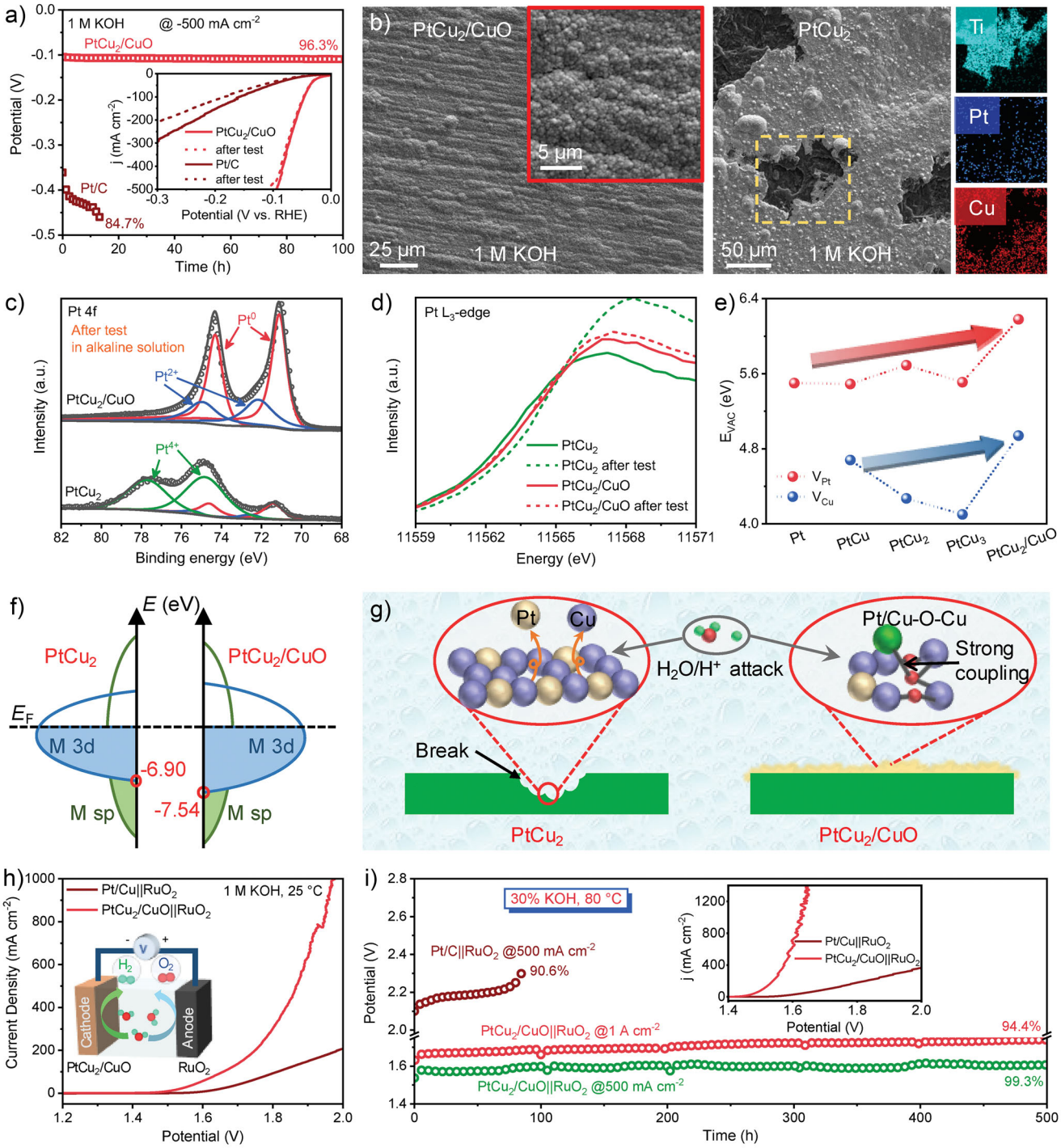

Figure 5. a) The chronopotentiometry curves for $PtCu_2/CuO$ and Pt/C in a 1 M KOH solution at a current density of −500 mA cm^{-2}, as well as the corresponding LSV curves before and after testing (see inset). b) SEM images for $PtCu_2/CuO$ and $PtCu_2$ after durability testing in a 1 M KOH solution, and EDS-mapping analysis was performed on the damaged areas of the $PtCu_2$ coating. c) XPS fine spectra for the Pt 4f of $PtCu_2/CuO$ and $PtCu_2$ coatings after testing in an alkaline solution. d) XANES spectra for $PtCu_2/CuO$ and $PtCu_2$ before and after testing in an alkaline solution. e) Vacancy formation energies for Pt and Cu atoms on Pt, PtCu, $PtCu_2$, $PtCu_3$ and $PtCu_2/CuO$. f) DOS schematic diagram illustrating the effect of heterostructures on hybridization between 3d orbitals and sp orbitals. g) Schematic diagram of $PtCu_2$ and $PtCu_2/CuO$ coatings resisting H_2O/H^+ attack. h) LSV curves for two-electrode electrolyzers with $PtCu_2/CuO$ cathode and RuO_2 anode ($PtCu_2/CuO||RuO_2$), respectively, for OWS in 1 M KOH. i) OWS performance and stability of $PtCu_2/CuO||RuO_2$ combination in a simulated industrial environment (30% KOH, 30 °C).

© 2025 Wiley-VCH GmbH

indicating that the low-valence Pt has been severely oxidized, consistent with the XPS analysis (Figure S32). Furthermore, the vacancy formation energies (E_{VAC}) for Pt and Cu atoms in Pt, PtCu, $PtCu_2$, $PtCu_3$ and $PtCu_2$/CuO were calculated using DFT methods, where Pt and Cu atoms located on the $PtCu_2$ side near CuO were selected in $PtCu_2$/CuO. The calculations indicate that both Pt and Cu in $PtCu_2$/CuO exhibit the largest E_{VAC} values, which helps to prevent atomic dissolution and agglomeration (Figure 5e). The DOS results presented in Figure 5f indicate that the $PtCu_2$/CuO heterojunction leads to stronger d-d/sp hybridization and more delocalized d-DOS, thereby enhancing the bonding between Pt and Cu atoms. Therefore, when the $PtCu_2$ coating faces long-term attack from H_2O/H^+ during the pH-universal HER process, it is prone to Pt/Cu atomic dissolution or agglomeration, ultimately leading to coating damage (Figure 5g). On the contrary, the Pt/Cu atoms in the $PtCu_2$/CuO coating exhibit excellent durability when subjected to the attack under the same conditions due to the electronic structure control and strong interaction brought about by the Pt/Cu—O—Cu ligand at the heterojunction interface.

To further manifest the excellent HER performance of $PtCu_2$/CuO in industrial alkaline electrolyzers, a two-electrode hydrolysis cell was assembled by combining a $PtCu_2$/CuO cathode with a commercial RuO_2 anode, and compared with a commercial Pt/C||RuO_2 combination. At room temperature, the LSV curves shown in Figure 5h indicate that the overall water splitting (OWS) performance of the $PtCu_2$/CuO||RuO_2 combination is significantly better than that of the commercial Pt/C||RuO_2 combination. Of note, the gap between them rapidly widens with increasing current density. Specifically, the $PtCu_2$/CuO||RuO_2 combination only requires cell voltages of 1.50, 1.66 and 1.86 V to achieve current densities of 10, 100 and 500 mA cm^{-2}, respectively, compared to that for the Pt/C||RuO_2 combination that requires cell voltages of 1.61, 1.81 and 2.35 V to achieve the same current densities (Figure S33). More encouragingly, these voltages have also been shown to perform well in recently reported advanced OWS electrocatalysts (Figure S34 and Table S3). Considering that industrial alkaline water electrolysis is typically carried out in high-temperature and high concentration solutions, further tests were conducted on the OWS performance and stability of the above two combinations in a 30% KOH electrolyte at 80 °C, and the results are shown in Figure 5i. Evidently, the OWS performance of $PtCu_2$/CuO||RuO_2 is much better than that of commercial Pt/C||RuO_2 (inset in Figure 5i). Meanwhile, this combination can operate continuously for more than 500 h without performance degradation at a high current density of 500 mA cm^{-2}, and its OWS performance can still be maintained at 94.4% at a higher current density (1 A cm^{-2}) after 500 h, demonstrating promising industrial application prospects compared with advanced OWS electrocatalysts (Table S3).

Conclusion

In summary, a $PtCu_2$/CuO heterojunction electrocatalytic coating was designed to address the limited activity and stability of Pt-based electrocatalysts in alkaline HER processes. The electrochemical test results indicate that the as-prepared coating only requires overpotentials of 10, 14 and 47 mV to achieve a 10 mA cm^{-2} current density in, respectively, alkaline, acidic and neutral electrolytes, demonstrating excellent pH-universal HER activity. More importantly, the dual-electrode hydrolysis cell prepared from this coating can exhibit extremely low overpotential and excellent long-term stability under large current densities (only a 5.6% decrease after 500 hours of testing at 1 A cm^{-2}) in a simulated industrial environment. The unique asymmetric hexagonal ring structure located at the heterojunction interface provides strong support for the excellent HER activity and good stability. Specifically, the Cu sites located on the CuO side promote the movement of adsorbed H_2O^* away from the Fermi level by reducing the gap with free H_2O, and thus greatly enhancing the adsorption and dissociation for H_2O. Meanwhile, the asymmetric Pt—O—Cu ligand accelerates the electron transfer at the interface, effectively balancing the adsorption and desorption of H* by Pt sites. In addition, a stronger d-d/sp hybridization and more delocalized d-DOS can be found in the designed heterostructure, which is beneficial for increasing the energy of vacancy formation and enhancing interatomic interactions to prevent atomic dissolution and aggregation. The clear delineation in behavior at the heterojunction interface ensures the high HER activity to occur with stability. We hope that the above work can provide unique insights and guidance for the design of Pt-based electrocatalytic materials for practical hydrogen production.

Acknowledgements

This work is supported by the National Nature Science Foundation of China (Grant No. 52075245, 92472117, 22075141 and 52371226) and the Open Foundation of Shanghai Jiao Tong University Shaoxing Research Institute of Renewable Energy and Molecular Engineering (Grant No. JDSX2023019).

Conflict of Interests

The authors declare no conflict of interest.

Data Availability Statement

The data that support the findings of this study are available from the corresponding author upon reasonable request.

Keywords: Heterostructure · Hydrogen evolution reaction · Industrial electrolyzer · pH-universal · Pt-based catalysts

[1] Y. Feng, Y. Xie, Y. Yu, Y. Chen, Q. Liu, H. Bao, F. Luo, S. Pan, Z. Yang, *Angew. Chem. Int. Ed.* **2025**, *64*, e202413417.
[2] X. Liu, P. Liao, W. Liao, S. Wang, G. Li, *EnergyChem* **2025**, *7*, 100146.

© 2025 Wiley-VCH GmbH

[3] A. H. Shah, Z. Zhang, C. Wan, S. Wang, A. Zhang, L. Wang, A. N. Alexandrova, Y. Huang, X. Duan, *J. Am. Chem. Soc.* **2024**, *146*, 9623–9630.
[4] S. Li, G. Xing, S. Zhao, J. Peng, L. Zhao, F. Hu, L. Li, J. Wang, S. Ramakrishna, S. Peng, *Natl. Sci. Rev.* **2024**, *11*, 1.
[5] S. Zhou, W. Cao, L. Shang, Y. Zhao, X. Xiong, J. Sun, T. Zhang, J. Yuan, *Nat. Commun.* **2025**, *16*, 1849.
[6] Y. Feng, W. Zhu, J. Xu, D. Zhang, Q. Ma, L. Zhao, L. Lin, Q. Su, Y. Wang, Q. Liu, Y. Wei, X. Li, J. Huang, Y. Ye, J. Zhao, B. Wu, *ACS Nano* **2025**, *19*, 7948–7961.
[7] S. Zhu, X. Qin, Y. Yao, M. Shao, *J. Am. Chem. Soc.* **2020**, *142*, 8748–8754.
[8] Z. Chen, M. Yang, Y. Li, W. Gong, J. Wang, T. Liu, C. Zhang, S. Hou, G. Yang, H. Li, Y. Jin, C. Zhang, Z. Tian, F. Meng, Y. Cui, *Nat. Commun.* **2025**, *16*, 418.
[9] A. Goyal, M. T. M. Koper, *Angew. Chem. Int. Ed.* **2021**, *60*, 13452–13462.
[10] W. Shao, Z. Xing, X. Xu, D. Ye, R. Yan, T. Ma, Y. Wang, Z. Zeng, B. Yin, C. Cheng, S. Li, *J. Am. Chem. Soc.* **2024**, *146*, 27486–27498.
[11] Z. Ni, C. Luo, B. Cheng, P. Kuang, Y. Li, J. Yu, *Appl. Catal. B-Environ.* **2023**, *321*, 122072.
[12] G. Gao, G. Zhu, X. Chen, Z. Sun, A. Cabot, *ACS Nano* **2023**, *17*, 20804–20824.
[13] N. K. Chaudhari, Y. Hong, B. Kim, S.-I. Choi, K. Lee, *J. Mater. Chem. A* **2019**, *7*, 17183–17203.
[14] X. Rong, D. Xiao, Q. Li, Y. Niu, F. Ding, X. Hou, Q. Wang, J. Xu, C. Zhao, D. Zhou, R. Xiao, X. Yu, W. Yin, L. Gu, H. Li, X. Huang, L. Chen, Y.-S. Hu, *eScience* **2023**, *3*, 100159.
[15] M. Zhou, Y. Zhao, X. Zhao, P.-F. Yin, C.-K. Dong, H. Liu, X.-W. Du, J. Yang, *ACS Appl. Energy Mater.* **2024**, *7*, 3848–3857.
[16] J. Chen, G. Qian, H. Zhang, S. Feng, Y. Mo, L. Luo, S. Yin, *Adv. Funct. Mater.* **2022**, *32*, 2107597.
[17] H. Zhang, R. Hu, S. Feng, Z. Lin, M. Zhu, *eScience* **2023**, *3*, 100080.
[18] Y.-W. Peng, C. Shan, H.-J. Wang, L.-Y. Hong, S. Yao, R.-J. Wu, Z.-W. Zhang, T.-B. Lu, *Adv. Energy Mater.* **2019**, *9*, 1900597.
[19] K. Wang, S. Wang, K. S. Hui, J. Li, C. Zha, D. A. Dinh, Z. Shao, B. Yan, Z. Tang, K. N. Hui, *Adv. Funct. Mater.* **2023**, *33*, 2211273.
[20] X. Zhou, X. Liu, J. Zhang, C. Zhang, S. J. Yoo, J.-G. Kim, X. Chu, C. Song, P. Wang, Z. Zhao, D. Li, W. Zhang, W. Zheng, *Carbon* **2020**, *166*, 284–290.
[21] Z. Yang, C. Zhao, Y. Qu, H. Zhou, F. Zhou, J. Wang, Y. Wu, Y. Li, *Adv. Mater.* **2019**, *31*, 1808043.
[22] P. S. Lamoureux, A. R. Singh, K. Chan, *ACS Catal.* **2019**, *9*, 6194–6201.
[23] C. Zhang, X. Liang, R. Xu, C. Dai, B. Wu, G. Yu, B. Chen, X. Wang, N. Liu, *Adv. Funct. Mater.* **2021**, *31*, 2008298.
[24] R. Kronberg, K. Laasonen, *ACS Catal.* **2021**, *11*, 8062–8078.
[25] A. Wong, Q. Liu, S. Griffin, A. Nicholls, J. R. Regalbuto, *Science* **2017**, *358*, 1427–1430.
[26] W. Guo, Z. Wang, X. Wang, Y. Wu, *Adv. Mater.* **2021**, *33*, 2004287.
[27] Y. Yang, Z. Jia, Q. Wang, Y. Liu, L. Sun, B. Sun, J. Kuang, S. Dai, J. He, S. Liu, L. Duan, H. Tang, L.-C. Zhang, J. J. Kruzic, J. Lu, B. Shen, *Energy Environ. Sci.* **2024**, *17*, 5854–5865.
[28] B. Yan, X. Qin, T. Chen, Z. Teng, D. K. Cho, H. W. Lim, H. Hong, Y. Piao, L. Xu, J. Y. Kim, *Adv. Funct. Mater.* **2024**, *34*, 2309264.
[29] B. Pang, X. Liu, T. Liu, T. Chen, X. Shen, W. Zhang, S. Wang, T. Liu, D. Liu, T. Ding, Z. Liao, Y. Li, C. Liang, T. Yao, *Energy Environ. Sci.* **2022**, *15*, 102–108.
[30] H. Zhang, P. Song, P. Yao, D. Zhang, J. Cao, X. Gong, C. Han, W. Xu, *Chem. Eng. J.* **2023**, *470*, 144375.
[31] C. Liu, Q. Zhao, Y. Liu, S. Wang, E. W. Abel, *Colloids Surf. B* **2008**, *61*, 182–187.
[32] Y. Liu, Y. Su, J. Guan, J. Cao, R. Zhang, M. He, K. Gao, L. Zhou, Z. Jiang, *Adv. Funct. Mater.* **2018**, *28*, 1706545.
[33] Q. Yu, H. Huang, R. Chen, P. Wang, H. Yang, M. Gao, X. Peng, Z. Ye, *Nanoscale* **2012**, *4*, 2613.
[34] Y. Wang, X. Li, M. Zhang, Y. Zhou, S. Rao, C. Zhong, J. Zhang, X. Han, W. Hu, Y. Zhang, K. Zaghib, Y. Wang, Y. Deng, *Adv. Mater.* **2020**, *32*, 2000231.
[35] K. Jayasayee, J. A. R. V. Veen, T. G. Manivasagam, S. Celebi, E. J. M. Hensen, F. A. de Bruijn, *Appl. Catal. B-Environ.* **2012**, *111–112*, 515–526.
[36] Q. Liu, J. Xian, Y. Li, Q. Zhang, H. Kitagawa, G. Li, *CCS Chem* **2022**, *4*, 3275–3284.
[37] X. Liu, G. Liu, L. Wang, Y. Li, Y. Ma, J. Ma, *J. Power Sources* **2016**, *312*, 199–206.
[38] W. Wang, Y. Wang, R. Yang, Q. Wen, Y. Liu, Z. Jiang, H. Li, T. Zhai, *Angew. Chem.* **2020**, *132*, 17122–17129.
[39] J. Xian, S. Li, H. Su, P. Liao, S. Wang, Y. Zhang, W. Yang, J. Yang, Y. Sun, Y. Jia, Q. Liu, Q. Liu, G. Li, *Angew. Chem. Int. Ed.* **2023**, *62*, e202304007.
[40] S. Fang, X. Zhu, X. Liu, J. Gu, W. Liu, D. Wang, W. Zhang, Y. Lin, J. Lu, S. Wei, Y. Li, T. Yao, *Nat. Commun.* **2020**, *11*, 1029.
[41] J. Xian, S. Li, H. Su, P. Liao, S. Wang, R. Xiang, Y. Zhang, Q. Liu, G. Li, *Angew. Chem. Int. Ed.* **2023**, *62*, e202306726.
[42] M. Singh, D. Paudel, H. Kim, T. Kim, J. Park, S. Lee, *Energy Adv.* **2025**, *4*, 716–742.
[43] Z. Li, P. Yu, D. Shen, X. Zhang, Z. Liang, B. Wang, L. Wang, *Chin. Chem. Lett.* **2025**, *36*, 109713.
[44] J. Yang, J. Feng, Y. Cao, Y. Xiao, L. Qiao, K. An, J. Yang, J. Peng, H. Pan, H.-M. Cheng, *Adv. Funct. Mater.* **2024**, *34*, 2411081.
[45] S. Wang, Y. Cao, W. Jia, Z. Lu, D. Jia, *Appl. Catal. B-Environ.* **2021**, *298*, 120579.

Manuscript received: May 10, 2025
Revised manuscript received: May 29, 2025
Accepted manuscript online: June 10, 2025
Version of record online: June 18, 2025

© 2025 Wiley-VCH GmbH